Applied Thermal Engineering 212 (2022) 118573

Contents lists available at ScienceDirect

Applied Thermal Engineering

journal homepage: www.elsevier.com/locate/apthermeng

Research Paper

Novel methods for measuring the thermal diffusivity and the thermal conductivity of a lithium-ion battery

Gavin White, Alastair Hales, Yatish Patel, Gregory Offer *

Department of Mechanical Engineering, Imperial College London, London, SW7 2AZ, United Kingdom

ARTICLE INFO

Keywords:
Lithium-ion battery
Thermal conductivity
Thermal diffusivity

ABSTRACT

Thermal conductivity is a fundamental parameter in every battery pack model. It allows for the calculation of internal temperature gradients which affect cell safety and cell degradation. The accuracy of the measurement for thermal conductivity is directly proportional to the accuracy of any thermal calculation. Currently the battery industry uses archaic methods for measuring this property which have errors up to 50 %. This includes the constituent material approach, the Searle's bar method, laser/Xeon flash and the transient plane source method. In this paper we detail three novel methods for measuring both the thermal conductivity and the thermal diffusivity to within 5.6 %. These have been specifically designed for bodies like lithium-ion batteries which are encased in a thermally conductive material. The novelty in these methods comes from maintaining a symmetrical thermal boundary condition about the middle of the cell. By using symmetric boundary conditions, the thermal pathway around the cell casing can be significantly reduced, leading to improved measurement accuracy. These novel methods represent the future for thermal characterisation of lithium-ion batteries. Continuing to use flawed measurement methods will only diminish the performance of battery packs and slow the rate of decarbonisation in the transport sector.

1. Introduction

Battery electric vehicles using renewable electricity can significantly reduce transport carbon dioxide emissions. Moreover, by maximising the usable life of electric vehicles the carbon footprint can be reduced further. A recent study by Lander *et al.* has shown that increasing battery pack lifetime, through optimal thermal management design, can significantly decrease the carbon footprint and cost of the battery pack by 25 % and 27 % respectively [1]. This is because an optimised battery thermal management system (BTMS) will minimise battery pack temperature gradients and in turn reduce current inhomogeneity [2]. Current inhomogeneity caused by temperature gradients can be linked directly to battery pack degradation rate as evidenced by Hunt *et al.* [3]. This study showed that temperature gradients can reduce lithium-ion battery pack lifetime by as much as 66 %. An effective BTMS will increase battery pack lifetime through minimisation of these temperature gradients.

BTMS's are heavily reliant on thermal models and are designed using them. This includes thermal models of the components in the battery packs including thermal models of the individual cells. These thermal models allow BTMS to be simulated and optimised throughout the design process. Cell thermal models also allow simulation of the cells thermal performance which can be used to optimise cell design. Additionally, these cell and pack models can also be used in adaptive control systems running in real-time on the battery management system. This improves the BTMS performance in application as well as initial design. Having accurate models will therefore improve BTMS leading to reduced pack temperature gradients.

Predictions of internal temperature gradients, shown in Fig. 1, are governed by thermal conductivity. Where the temperature profile through a 1D plane wall generating heat is given by the heat equation [4],

$$\frac{\partial^2 T}{\partial x^2} + \frac{\dot{e}_{gen}}{k} = \frac{1}{\alpha}\frac{\partial T}{\partial t} \tag{1}$$

where T is temperature [K], x is the distance from the mid plane [m], $\dot{e}_{gen}$ is the volumetric heat generation [W/m^3], k is the thermal conductivity [W/m.K], α is the thermal diffusivity [m^2/s] and t is time [s]. In this form the heat equation assumes that the heat generation is uniform throughout its volume which is a reasonable assumption under

* Corresponding author at: Department of Mechanical Engineering, Imperial College London, Exhibition Road, South Kensington, London, SW7 2AZ, United Kingdom.
E-mail address: Gregory.offer@imperial.ac.uk (G. Offer).

https://doi.org/10.1016/j.applthermaleng.2022.118573
Received 3 December 2021; Received in revised form 11 April 2022; Accepted 21 April 2022
Available online 26 April 2022

Nomenclature

T	Temperature [K]
x	Distance [m]
$\dot{e}_{gen}$	Heat generated per unit volume [W/m^3]
k	Thermal conductivity [W/m.K]
α	Thermal diffusivity [m^2/s]
t	Time [s]
L	Characteristic length – half the wall thickness [m]
ρ	Density [kg/m^3]
c_p	Specific heat capacity [J/kg.K]
e	Thermal Effusivity [W.s$^{1/2}$/m^2.K]
X	Independent spatial variable
ψ	Independent time variable
A	Constant
B	Constant
C	Constant
a_n	Fourier coefficient
π	Pi
∞	Infinity
τ	Time constant [s]
$\dot{q}$	Surface heat flux rate [W/m^2]
$\dot{Q}$	Heat generation rate [W]
V	Volume [m^3]
R_θ	Thermal resistance [K/W]
A_1	Cross-sectional area [m^2]
k_θ	Average thermal conductivity [W/m.K]

Superscript and subscripts

n	Integer number
Av	Average
0	Initial of variable

Abbreviations

BTMS	Battery thermal management system
LFP	Lithium iron phospate
TPS	Transient plane source
MTPS	Modified transient place source
1D	One-dimensional
PID	Proportion integral derivative (controller)

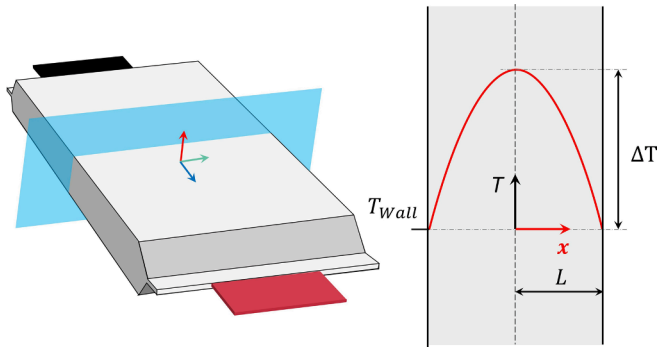

Fig. 1. Example of steady state internal temperature gradient in a pouch cell (1D plane wall).

prescribed cycling conditions such as square wave pulsing. A detailed analysis of the sources of heat generation in a battery system is presented in Berardi *et al.* which can be used as an input to this model [5]. By differentiating the heat equation at steady state it can be shown that the maximum temperature difference,ΔT [K] is given by

$$\Delta T = \frac{\dot{e}_{gen} L^2}{2k} \tag{2}$$

where L is half the wall thickness [m].

Equation (2) shows that the maximum internal temperature difference is inversely proportional to the thermal conductivity. Therefore, any error in the thermal conductivity will be carried into the maximum predicted temperature. Currently there are two approaches for measuring the thermal conductivity of a lithium-ion cell:

1. Average of the constituent material properties
2. Direct measurement of lumped thermal conductivity

The first approach to use the constituent materials is flawed due to the difficulties in accounting for thermal contact resistance [6]. Measuring the thermal contact resistance at the interface of any two layers requires the cell to be disassembled [7]. This is challenging and will lead to large errors because the electrolyte will evaporate during disassembly, increasing the apparent contact resistance and thus reducing the calculated thermal conductivity. Bazinski et al. found a significant increase of 92 % in thermal conductivity for a Lithium iron phosphate (LFP) pouch cell in the presence of electrolyte [8]. Often the thermal contact resistance is not even included in the equivalent thermal resistance calculations, with material properties taken from Maleki *et al.* and perfect contact between layers incorrectly assumed. The experimental difficulty in measuring these contact resistances compounded with the many layers within a cell make the measurement uncertainties large and the conductivity values error prone.

The second approach which uses a direct measurement of the thermal conductivity accounts for the individual contact resistances because they are included in the lumped parameter. Several thermal property measurement methods, originally intended for homogenous/composite bodies, have been applied to batteries and can be split into steady state and transient methods. For steady state methods the heat flow is allowed to equilibrate before the thermal conductivity is determined. This method was used by Werner *et al.* which was a detailed study for the technology available at the time [9]. Transient methods differ in that the time dependent temperature response is used to measure either the thermal diffusivity or the thermal effusivity. A good example of this is the study by Maleki *et al.* in what was a comprehensive study for its time [10]. Thermal diffusivity, α [m^2/s] and thermal effusivity, e [W.s$^{1/2}$/m^2.K] dictate the time dependent response of a body and are related to the thermal conductivity, k [W/m.K] through.

$$\alpha = \frac{k}{\rho c_p} \tag{3}$$

and

$$e = \sqrt{k \rho c_p} \tag{4}$$

respectively. Measuring either the thermal diffusivity or thermal effusivity therefore allows simple calculation of the thermal conductivity when the density and specific heat capacity are known. This allows the thermal conductivity to be measured using a transient response.

The difference between the direct measurement methods applied to batteries are quite acute. Fig. 2(a) summarises these methods and highlights the differences between them. The guarded hot plate is the only steady state method shown and involves measuring the thermal gradient when a known heat source is applied to one side of the body. Laser/Xeon flash is a transient method which has been continuously developed since its original proposition by Parker *et al.* [11]. A pulse of

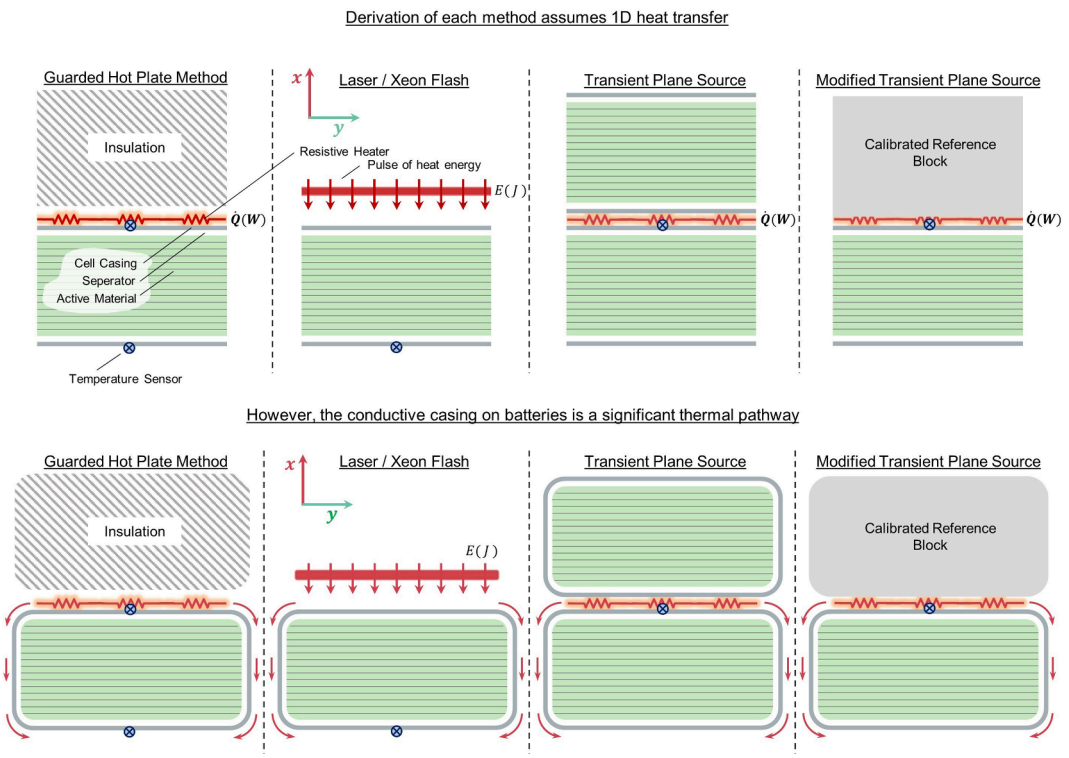

Fig. 2. (a) Idealised 1D heat transfer assumed in the guarded hot plate, laser/xeon flash, transient and modified transient plane source methods. (b) Section view of a pouch cell which shows how the conductive casing of the batteries acts as an alternate thermal pathway.

heat is applied to one side of a body by either a laser or a Xeon flash tube and both the speed and magnitude of the response on the other side can be used to determine the thermal conductivity and specific heat capacity. The transient plane source (TPS) also uses the transient temperature response of the body with the sensors and heat source on the same side of the body. The TPS method requires the sensor to be sandwiched between two identical samples and can be used to measure the thermal conductivity and thermal effusivity. The modified transient plane source (MTPS) is very similar to the TPS but instead of being sandwiched between two identical samples, it uses a calibrated reference block, simplifying the measurement procedure.

Each of these methods assume ideal 1D heat flow, but in reality the heat flow is multi-dimensional leading to large errors. Fig. 2(a) shows the assumed 1D heat flow along the x-axis for four different methods where the heat flow in both the y-axis and z-axis is negligible. Fig. 2(b) demonstrates the actual heat flow when these methods are applied to batteries. A favourable heat path around the cell along the y-axis exists which causes an over estimation of the thermal conductivity. This is a significant source of error which varies from cell to cell and is a function of the cell form factor, casing size, thickness and material. Steinhardt *et al.* highlighted the magnitude of this error in a comprehensive thermal study of a 34 Ah prismatic cell [12]. This study showed that the thermal conductivity across the cell was reduced by 83.2 % when the heat flow around the sides and top of the cell were subtracted. Almost all studies do not try to account for this multi-dimensional heat flow which leads to poor thermal conductivity results.

This paper details three novel methods for measuring the thermal diffusivity of lithium-ion batteries which overcome the multi-dimension heat flow problem. These novel methods have been specifically designed for bodies like lithium-ion batteries which are encased in a thermally conductive material. The novelty in these methods comes from maintaining a symmetrical thermal boundary condition about the middle of the cell. This significantly reduces unwanted heat flow around the casing of the cell, thus improving the accuracy of the new methods.

2. Theory

There are three novel methods presented in this paper:

a) *The internal heating method:* Fitting the surface heat flux during the formation and collapse of a steady state internal temperature during and after a period of constant heat generation.
b) *The step change method:* Fitting the surface heat flux after a step change to the surface of a wall of the body.
c) *The heat stored method:* Equating the energy absorbed during the formation of a steady state temperature profile with the increase in average internal temperature.

Methods (a) and *(b)* utilise 1D analytical solutions to the heat equation which relate the surface heat flux response to the thermal diffusivity. Additionally, *method (c)* uses an energy balance to calculate the thermal diffusivity. The solutions for these methods are presented below.

2.1. Heat flux decay

The temperature profile through a 1D plane wall generating heat is given by [1]. In order to apply the separation of variables method, the forcing term $\left(\dot{e}_{gen}/k\right)$ is set equal to 0, i.e. when there is no internal heat generation. Although this limits the use of this method to situations where the temperature profile is collapsing, it can be shown that a temperature profile collapsing is the inverse solution of a temperature profile developing. Considering the collapse of a temperature profile yields.

$$T(x,t) = \mathrm{X}(x)\Psi(t) = [A\sin(sx) + B\cos(sx)]\exp^{-s^2at} \quad (5)$$

where A, B and s are constants and $\mathrm{X}(x)$ and $\psi(t)$ are the independent spatial and time components, respectively. Sections 2.1.1 and 2.1.2

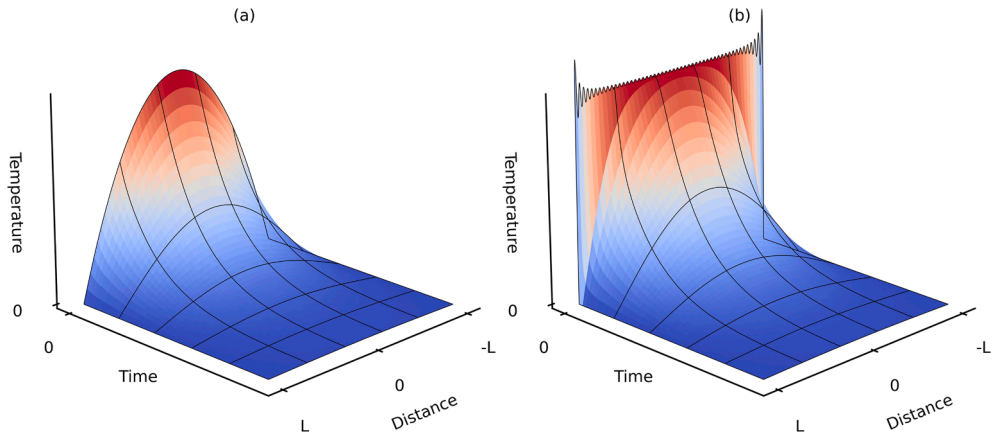

Fig. 3. Plots showing the temperature profile collapsing over time for method (a) a steady state temperature profile and (b) an instantaneous step change on the wall. Note the Gibbs phenomena for (b) from the Fourier series approximation of the step change.

describe how the constants can be solved for *methods (a)* and *(b)* with the solutions shown in Fig. 3.

2.1.1. Initial conditions – Fourier approximation

The collapse of the temperature profiles given in Fig. 3 can be analytically solved by applying known boundary conditions to Equation (5). The first of these are the initial conditions:

Method (a): The 1D steady state temperature profile equation.

$$T(x,0) = \frac{\dot{e}_{gen}}{2k}\left(L^2 - x^2\right) \tag{6}$$

Method (b): A step function.

$$T(x,0) = \begin{cases} 1, |x| \le L \\ 0, |x| > L \end{cases} \tag{7}$$

where L is half the body thickness [m]. Both initial conditions are then expressed as a Fourier series to capture the high frequency decay terms and to make a continuous function from Equation (7). To improve the quality of the series approximation the initial conditions were extended over the range $[-2L, 2L]$ and Equation (6) was shifted to be symmetric about $x = 0$ in the extended range. This was done specifically to improve the approximation at $x = \pm L$ which are the points of interest. This extension and shift yields the new piecewise functions: *Method (a)*:

$$T(x,0) = \begin{cases} (x+3L)(x+L), -2L \le x < -L \\ -(x+L)(x-L), -L \le x \le L \\ (x-3L)(x-L), L < x \le 2L \end{cases} \tag{8}$$

Method (b):

$$T(x,0) = \begin{cases} 1, -2L \le x < -L \\ -1, -L \le x \le L \\ 1, L < x \le 2L \end{cases} \tag{9}$$

Equations (8) and (9) are even about $x = 0$ and $T = 0$ respectively. The Fourier series equation reduces to Equation (10) where a_n is a Fourier coefficient and n is a positive integer.

$$f(x) = \sum_{n=1}^{\infty}\left(a_n \cos\left(\frac{n\pi x}{L}\right)\right) \tag{10}$$

By solving for the Fourier coefficient the piecewise functions in Equations (8) and (9) can be represented as Equations (11) and (12) respectively.

$$f(x) = T(0) = \frac{2\dot{e}_{gen}}{kL}\sum_{n=1}^{\infty}\left(\left(\frac{2L}{\pi n}\right)^3 \sin\left(\frac{\pi n}{2}\right).\cos\left(\frac{n\pi x}{L}\right)\right) \tag{11}$$

$$f(x) = T(0) = \sum_{n=1}^{\infty}\left(\left(\frac{4\Delta T}{\pi n}\right)\sin\left(\frac{\pi n}{2}\right)\cos\left(\frac{n\pi x}{L}\right)\right) \tag{12}$$

where ΔT is the magnitude of the step change on the walls.

2.1.2. Heat Equation solution

Equations (11) and (12 can then be used as the initial conditions to solve Equation (5) for *method (a)* and *(b)* respectively. The remaining boundary conditions describe how the temperature at the walls is fixed throughout time which is achieved using conduction and an adaptive Peltier control system. These boundary conditions are common for both methods and are given in Equations (13-15).

$$T(-L,t) = 0 \tag{13}$$

$$T(L,t) = 0 \tag{14}$$

$$T(L,0) = 0 \tag{15}$$

These initial conditions and boundary conditions yield the solutions, Equation (16) and (18) for the two methods. Presented also are the equations describing the gradient at the boundary $x = L$ which can be divided by the thermal conductivity to calculate the heat flux.

Method (a): The internal heating method – Temperature distribution during the collapse of a steady state temperature profile:

$$T(x,t) = \sum_{n=1,3,5\ldots}^{\infty}\left(\left(\frac{4}{L}\right)\left(\frac{2L}{\pi n}\right)^3 \sin\left(\frac{\pi n}{2}\right)cos(sx)\right)exp^{-\frac{t}{\tau}} \tag{16}$$

$$\frac{dT}{dx}(L) = \frac{\dot{q}}{k} = \sum_{n=1,3,5\ldots}^{\infty}\left(-\left(\frac{\dot{e}_{gen}L}{2k}\right)\left(\frac{4}{\pi n}\right)^2\right)exp^{-\frac{t}{\tau}} \tag{17}$$

Method (b): The step change method - Temperature distribution after a step change to both wall of the body:

$$T(x,t) = \sum_{n=1,3,5\ldots}^{\infty}\left(\left(\frac{4\Delta T}{\pi n}\right)\sin\left(\frac{\pi n}{2}\right)cos(sx)\right)exp^{-\frac{t}{\tau}} \tag{18}$$

$$\frac{dT}{dx}(L) = \frac{\dot{q}}{k} = \sum_{n=1,3,5\ldots}^{\infty}\left(-\frac{2\Delta T}{L}\right)exp^{-\frac{t}{\tau}} \tag{19}$$

Given:

$$\tau = \frac{1}{s^2\alpha} \tag{20}$$

$$s = \frac{n\pi}{2L} \tag{21}$$

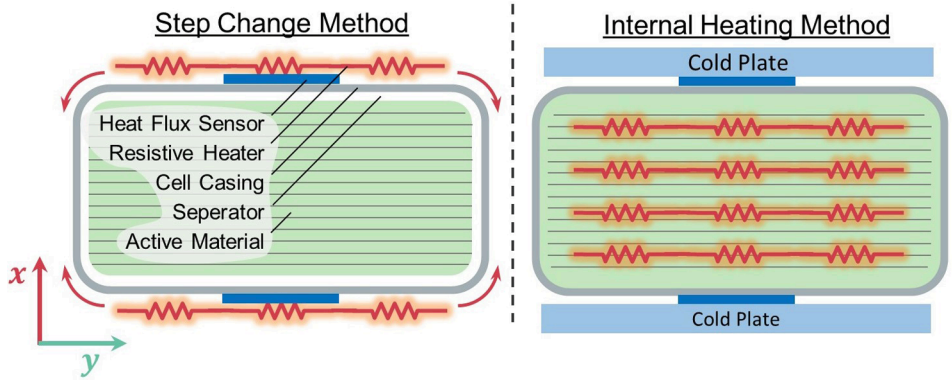

Fig. 4. Section view showing the symmetrical boundary conditions for the step change and internal heating methods for measuring thermal diffusivity and thermal conductivity.

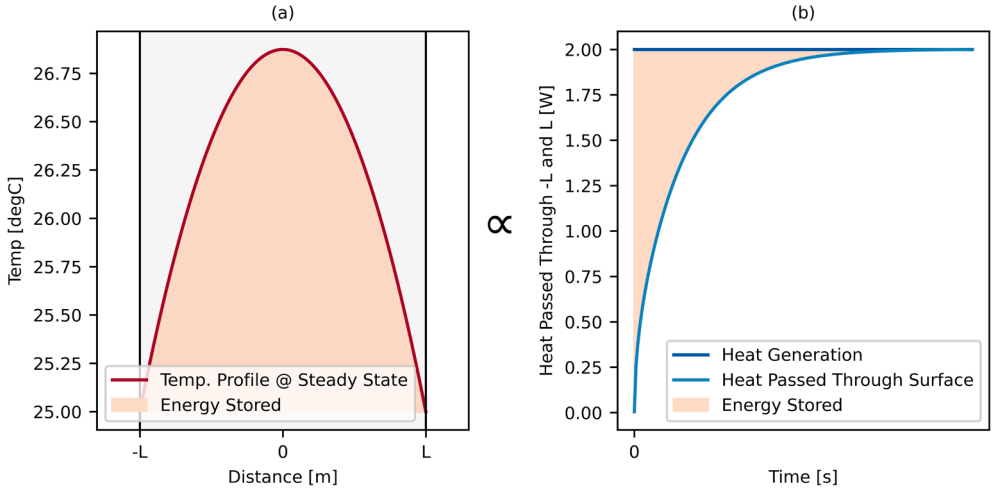

Fig. 5. Shaded regions indicate: (a) Proportional to the thermal energy stored under a steady state temperature profile. (b) Energy absorbed during formation of a steady state temperature profile.

where $\dot{q}$ is the surface heat flux rate [W/m^2] and n is now an odd positive integer.

The analytical solutions given in Equations (17) and (19) allow measurement of the thermal diffusivity, α, of a body through constrained curve fitting of the experimental heat flux response. This is significant because both methods (a) and (b) maintain a symmetric boundary condition about the centre of the body which removes the temperature gradient from one side of the body to the other. The removal of this temperature gradient prevents the undesired heat flow and associated errors that limit the accuracy of the traditional methods as discussed in section 1. The symmetric boundary conditions for methods (a) and (b) are shown in Fig. 4 which also highlights the key differences between the methods. The step change method uses no internal heating and instead uses temperature control plates which adjust both surfaces of the cell at the same time. In contrast the internal heating method uses temperature control plates to maintain both surfaces at the same temperature while using internal heating to generate a response in the heat flux sensors. Both methods result in less heat flow along the y-axis making the assumptions used in the derivation more representative.

Additionally, with measurements for the RHS of Equation (19) and a measurement of the surface heat flux $\dot{q}$, the thermal conductivity can be calculated. This is only the case for method (b), the step change method, as the multiplier for method (a) the internal heating method, does not contain the thermal conductivity. This allows the specific heat to be calculated from the relationship between thermal diffusivity and conductivity given by Equation (3) assuming the density is known (which can be measured using Archimedes principle not requiring expensive equipment).

2.2. Heat stored under steady state temperature profile

The thermal diffusivity can also be calculated using the heat stored method. This method seems rather abstract but is in fact a very simple energy balance. First, consider the heat stored under a steady state temperature profile. At steady state the temperature profile is given by Equation (6) which can be integrated between the walls to give

$$T_{Av} = \frac{\dot{e}_{gen} L^2}{3k} \tag{22}$$

where T_{Av} is the average temperature. The difference between the average temperature and the initial temperature can then be used to find the change in energy of the body using

$$\Delta E = mc_p(T_{Av} - T_0) \tag{23}$$

where ΔE is the change in energy and T_0 is the initial temperature of the body. Equation (23) describes the thermal energy stored under the temperature profile shown in Fig. 5 (a). It is the new average thermal energy minus the initial thermal energy of the body. The thermal energy described here is only completely stored under the temperature profile once the system has reached steady state. The system takes time to reach steady state as initially some of the heat energy is stored within the body and some of it is passed out of the surfaces at -L and L.

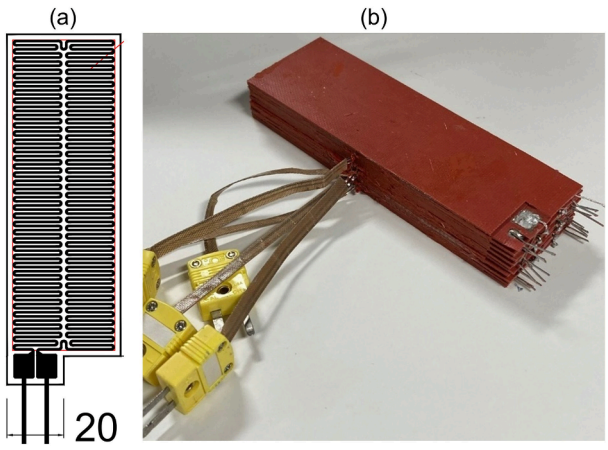

Fig. 6. Silicone block heater (a) internal heating foil design (b) heating block after individual heaters have been glued together.

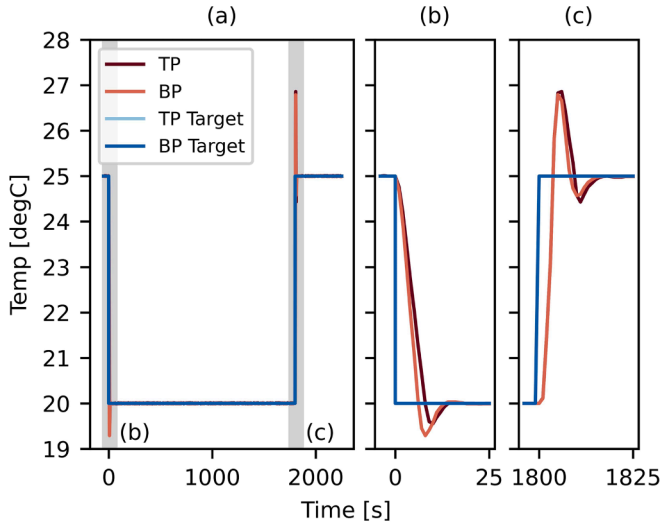

Fig. 7. Step change response of PID temperature control system.

Fig. 5 shows a plot of how much energy passes out of the surfaces at -L and L over time. It shows that over time the amount of heat leaving the surfaces increases until at $t = \infty$ the body is at steady state and all heat being generated leaves through the surfaces -L and L. As the heat generation over this time period is fixed at a constant the difference between the energy passing out of the surface at steady state and the energy actually being passed out must be the energy stored. Fig. 5 aims to gives a visual representation of the energy being equated which can be described as:

$$heat\ stored = heat\ generated - heat\ passing\ through\ surfaces \tag{24}$$

By recording the heat flux at the surface during this formation, it is possible to calculate the energy stored as equation (24) can be written as

$$\Delta E = \int \dot{Q}dt - \int \dot{q}dt \tag{25}$$

where $\dot{Q}$ is the heat generation rate [W]. Also, we know that

$$\dot{e}_{gen} = \frac{\dot{Q}}{V} \tag{26}$$

where V is the volume [m^3]. Equations (3), (25) and (26) can be substituted into Equation (23) and rearranged to give the thermal diffusivity:

$$\alpha = \frac{\dot{Q}L^2}{3\int \dot{Q}dt - \int \dot{q}dt} \tag{27}$$

This gives a simple way to calculate the thermal diffusivity given the heat generated and a record of the heat flux over time.

3. Experimental procedure

It was not possible to validate the novel methods presented in this paper on a real lithium-ion cell as traditional methods have an associated error from unwanted heat flow around the casing. Experimental validation of the new methods was therefore difficult as two of the three methods presented require uniform internal heat generation. This is impossible with typical reference samples as the electrical resistance is either too low, resulting in very little joule heating, or too high, resulting in very little current flow. To overcome these challenges, a bespoke silicone block heater was fabricated which provided volumetrically uniform heat generation without a conductive casing material. This meant that both the traditional and novel methods could be performed on the same sample without unwanted heat flow around the side.

3.1. Apparatus

The objective of the block heater was to create a volume that generated heat as uniformly as possible. This simulated the heat generation that is typically produced in a lithium-ion cell which also generates heat throughout its volume. The heater block was made from 20 individual silicone heaters glued together and each heater was only 0.80 mm thick. The internal foil design, shown in Fig. 6 (a), was optimised to produce as close to uniform heat generation as possible. To capture the internal temperature profile four flat leaf thermocouples were placed between the layers during gluing with an additional two added to the surface during testing. The heaters were electrically connected in a 2s10p configuration which resulted in a total resistance of 12.63 ohms. Before assembly of the block the resistance of each heater was measured with the standard deviation found to be 1.04 %.

A heat flux sensor was placed on either side of the block to provide a linear voltage response for increasing heat flux. The voltage response was calibrated for each setup using steady state. To ensure a constant amount of heat was generated during the experiments a Biologic potentiostat was used as a constant power source.

The presented methods also require accurate temperature control of the boundary conditions. For this a custom PID controller was made using Peltier elements which switch between heating and cooling in response to a thermistor placed on the cooling plate. The Peltier elements contact a cooling plate which is in direct contact with the surfaces of the sample. The controller was heavily optimised and tuned to allow for fast changes to the boundary conditions and quick responses to any changes in heat generation from the sample. Fig. 7 shows how the controller achieved the requested step changes in under 20 s. Over the course of a 30-minute relaxation these responses appear as an almost perfect step which is fundamental to achieve accurate measurements.

A rig was made to clamp the test device to the various sensors and cooling plates. It was made from machined aluminium plates which has cut outs and fixing holes to secure the key components. It also featured the copper cooling plates shown in Fig. 8 which were placed in contact with the faces of the heater block and the Peltier controller was used to precisely control the plate temperature. The heat from the Peltier controller was extracted using a water-cooling block and attached chiller system. As there are many layers of components in the construction of the rig, the thermal contact resistance between the heater and the cooling plate, which is known to be highly dependent on compression levels [13], could significantly influence the results. To mitigate these effects, a spring mechanism was used to maintain consistent clamping pressures. This reduced the contact resistances

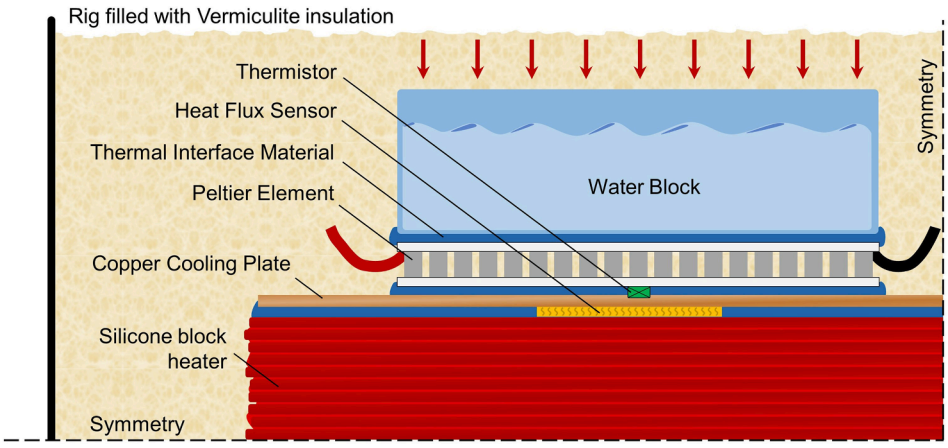

Fig. 8. Experimental setup for silicone block heater showing how the Peltier element is used to control the surface temperature of the silicone heater with a embedded heat flux sensor in-between.

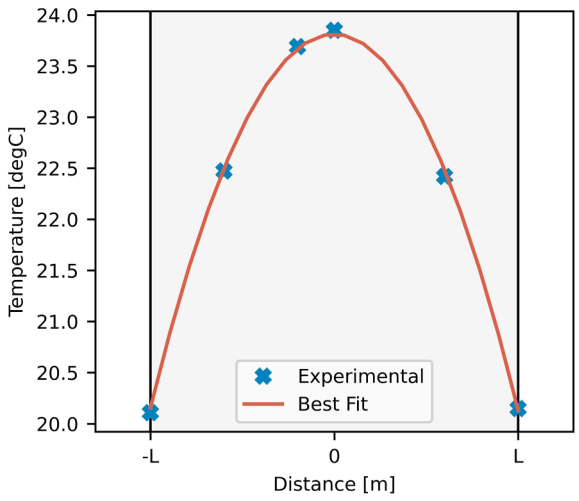

Fig. 9. Analytical steady state temperature profile fit to thermocouples at known positions through the thickness of the silicone block heater.

between each of the layers while ensuring that the maximum clamping pressure on the Peltier elements or the heat flux sensor was not exceeded.

The derivation of the analytical equations assumes that the heat transfer is 1D, i.e. the heat transfer in the other two dimensions is negligible. To ensure the experimental results reflect this, considerable effort went into minimising the heat loss through the ends and side of the device under test. This was achieved by placing the rig in a box and filling the box with 1–3 mm sized Vermiculite. This surrounded the exposed surfaces of the sample making the heat transfer negligible through the ends and sides. This strategy is completely transferable to testing with lithium-ion cells (indeed it also makes experiments with lithium-ion cells safer as vermiculite is a natural fire suppressant).

4. Reference thermal properties (Control)

To validate the accuracy of the new methods the thermal properties of the heater block were first determined through traditional established methods. Calorimetric methods were used to determine specific heat capacity, c_p. The heater block was encased in insulation and a potentiostat was used to provide constant power to the heater block in short bursts. The temperature rise of the block, as a consequence of the known energy passed into the block, was used to determine c_p. The accuracy of the determined value for c_p was improved during post processing. The losses from the block into the surrounding insulation during the experiment were determined from the rate of the temperature decay that occurred in the apparatus following the completion of each pulse. These losses were then accounted for when calculating c_p.

The thermal conductivity of the block heater was determined using the steady state internal temperature profile measured from the internal thermocouples. At steady state the temperature profile in a 1D body is given by Equation [6] which can be used to solve for the thermal conductivity, k, if the heat generation and temperatures at positions, x, through the body are known. To ensure the heater block was at steady state a constant amount of heat was generated using the Biologic potentiostat until the heater thermalised.

The best fit from the analytical equation is shown over the thermocouple measurements in Fig. 9. The thermocouples were grouped towards the centre of the body to improve the resolution when finding the maximum temperature.

4.1. Thermal properties from novel methods (a) - (c)

4.1.1. Test procedure

The rig was carefully assembled and clamped tight until the spring displacement gave the required clamping pressure of 0.3 MPa. All electrical connections and coolant connections were made before the rig was placed in a box. This was filled with Vermiculite and gently agitated until the insulation had filled all the small voids. The rig was placed in a climate chamber at 22.5 °C and left to thermalise for 8 h to provide an isothermal datum for the various thermistors and thermocouples. Following this the coolant flow was turned on followed by the Peltier control system with the thermal boundary against the heater set to 25 °C. This was left to rest for one hour before the following testing cycle started:

1. Step change of thermal boundary set point from 25 °C to 20 °C. Thermal boundary is maintained at 20 °C until Step 6.
2. Rest for 30 min.
3. Generate heat at a rate of 2 W in the resistance heater for a period of 30 min.
4. Instantly stop power generation.
5. Rest for 30 min.
6. Step change of thermal boundary set point from 20 °C to 25 °C.
7. Rest for 30 min

This procedure was repeated ten times to reduce the uncertainty in the result. Between each repeat the rig was completely dismantled, cleaned and reassembled.

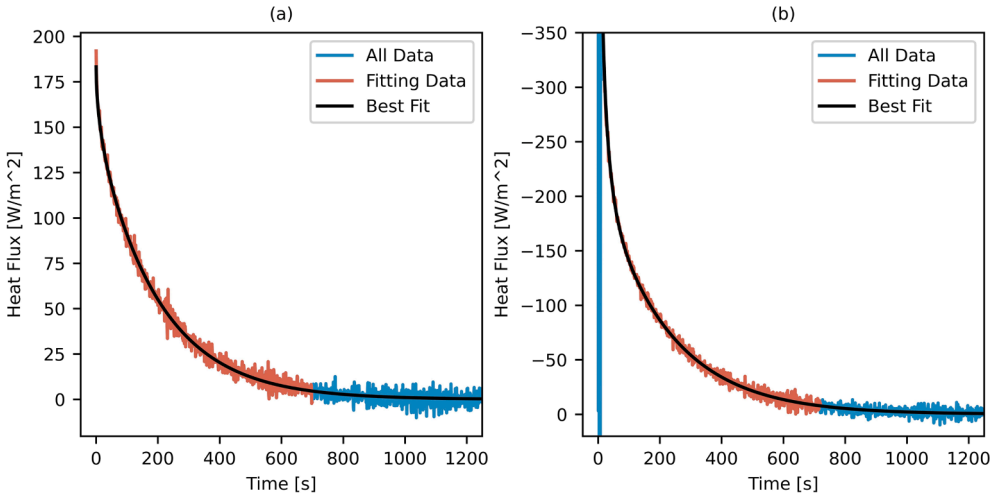

Fig. 10. Experimental decay of heat flux with lines of best fit for (a) method a. the internal heating method and (b) for method b. the step change method.

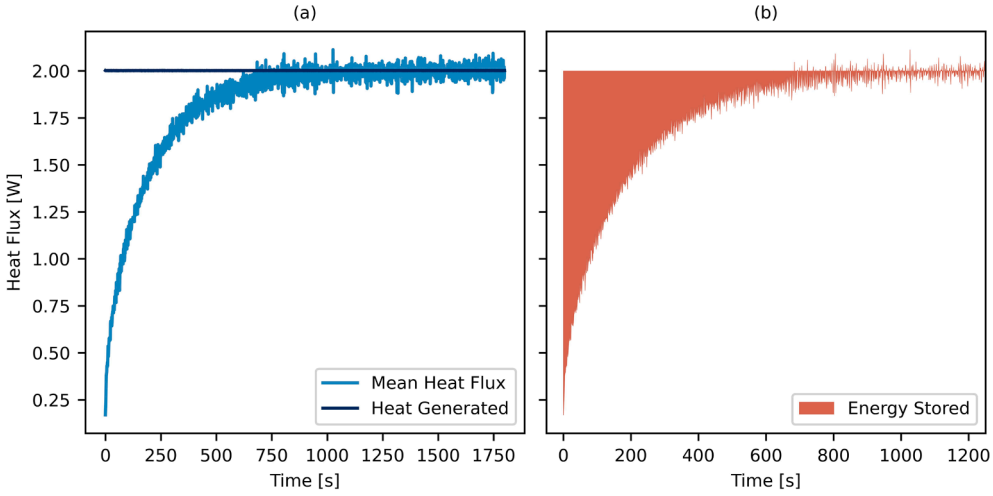

Fig. 11. Graphic highlighting the energy stored during the development of a steady state temperature profile.

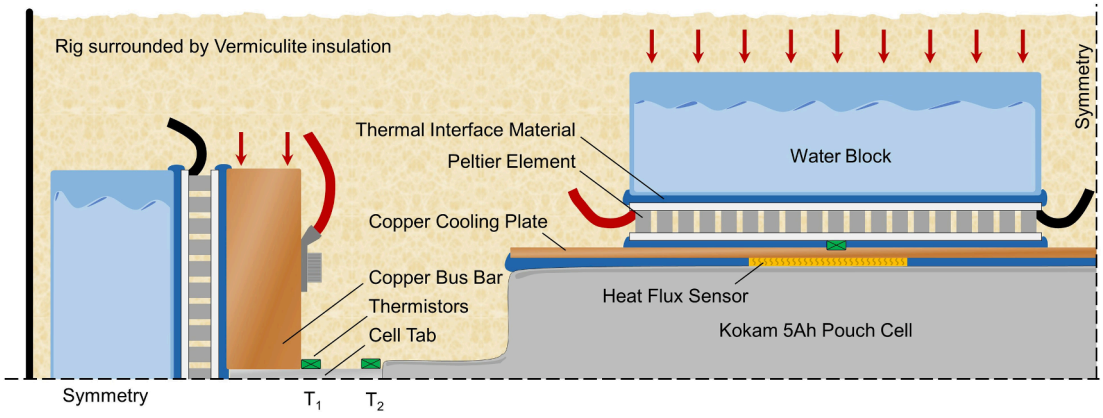

Fig. 12. Cross section view of main components in cell testing rig showing how the tab temperatures was controlled to reduce heat loss.

4.1.2. Data fitting

The heat flux sensors generate a voltage directly proportional to the heat flow through them. Using this, the heat flux sensors can be calibrated in the last few minutes of step 3 in the test procedure as the block heater can be considered at steady state. At steady state we know that.

$$\dot{q} = \dot{e}_{gen} L \tag{28}$$

with this calibration then applied over the whole voltage response.

The *Lmfit* Python library [14] was used to find the best fit between the measured heat flux and Equations [17] and [19]. Both equations

Table 1
Thermal properties of the silicone heater block from traditional methods.

Method Used	Material Property	Sample Mean	Units	Sample Standard Deviation
Calorimetry	Specific Heat Capacity	949.3	J/kg. K	1.23 %
Matching Internal Temperature Profile	Thermal Conductivity	0.2911	W/ m.K	6.05 %
Direct Measurement of Mass and Volume	Density	1581	Kg/ m^3	0.13 %
Calculated from Equation (20)	Thermal Diffusivity	0.1940x10^{-6}	m^2/s	6.27 %

Table 2
Thermal properties of the silicone heater block from the internal heating, step change and the energy stored methods.

Method Used	Thermal Diffusivity		Difference Between Sample Mean and Reference Value Sample Mean
	Sample Mean [m^2/s]	Sample Standard Deviation	
(a) Internal Heating	0.1831x10^{-6}	3.20 %	− 5.60 %
(b) Step Change on Boundary	0.1797x10^{-6}	3.43 %	− 7.34 %
(c) Energy Stored	0.2161x10^{-6}	5.86 %	11.4 %

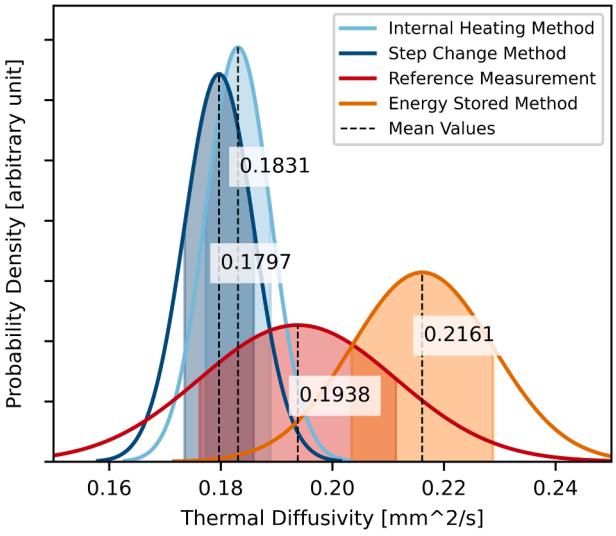

Fig. 13. Plots of the estimated mean and estimated standard deviation for the internal heating, step change and the energy stored methods. Shaded region shows a range of 1σ or one standard deviation.

Table 3
Direct measurement of the thermal conductivity of the silicone heater block using the magnitude of the heat flux response during the step change.

Method Used	Thermal Conductivity Sample Mean [W/m. K]	Sample Standard Deviation	Difference Between Sample Mean and Reference Value Sample Mean
Step Change on Boundary	0.2289	2.60 %	−21.35 %

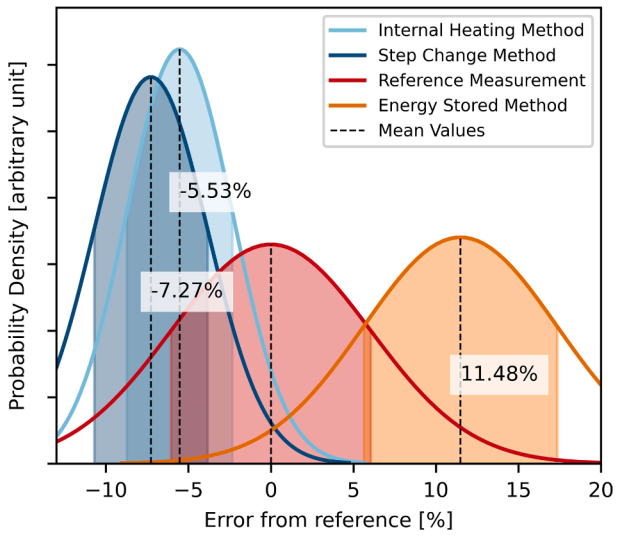

Fig. 14. Plots of the estimated mean and standard deviation for both the direct measurement of thermal conductivity and also the calculated thermal conductivity from the diffusivity. Shaded region shows a range of 1σ or one standard deviation.

Table 4
Measured thermal diffusivity and calculated thermal conductivity for a Kokam 5 Ah pouch cell.

Method Used	Sample Mean		Sample Standard Deviation
	Thermal Diffusivity [m^2/s]	Thermal Conductivity [W/m. K]	
(a) Internal Heating	0.8390x10^{-6}	1.366	7.82 %
(b) Step Change on Boundary	0.9048 x10^{-6}	1.473	6.34 %

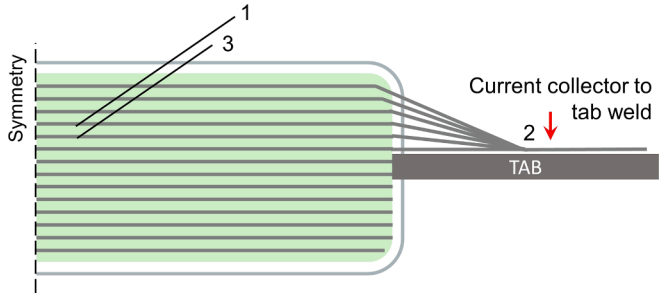

Fig. 15. Simplified cross-section view of a pouch cell including the current collector to tab weld.

show that the shape of the decay is governed by only the series exponential term with the multiplication constants governing the magnitude of the decay. For the internal heating method, the multiplication constants offer no insight into the thermal properties so they were replaced with a fitting constant c_1, shown in Equation [29]. c_1 and α were both used as the fitting parameters for the internal heating method allowing measurement of α. For the step change method the data was fit to Equation [30] allowing k and α to be the fitting parameters allowing measurement of them both.

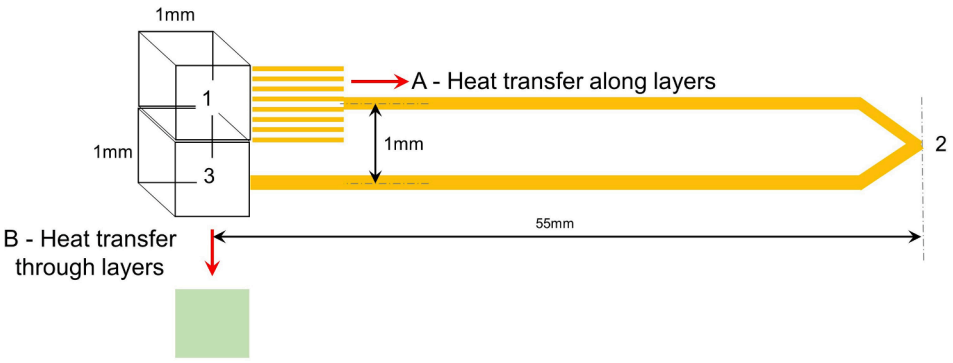

Fig. 16. Simplification of thermal pathways A and B within a pouch cell.

Table 5
Comparison of thermal resistance. * from the centre of the cell to the tab and then back again ** from the centre of one element to the centre of another.

	Pathway A	Pathway B
k_θ [W/m.K]	1.37	19.7
Δx [m]	$1.00x10^{-3}$**	$55.0x10^{-3}$ x2*
R_θ [% of total]	11.6	88.4
Relative Heat Flow [%]	**88.4**	**11.6**

5. Method (a): The internal heating method:

$$\dot{q} = c_1 \sum_{n=1,3,5\cdots}^{\infty} \left(\frac{1}{n}\right)^2 exp^{-\frac{t}{\tau}} \tag{29}$$

6. Method (b): The step change method:

$$\dot{q} = k \sum_{n=1,3,5\cdots}^{\infty} \left(-\frac{2\Delta T}{L}\right) exp^{-\frac{t}{\tau}} \tag{30}$$

Where:

$$\tau = \frac{1}{s^2 \alpha} \tag{31}$$

The experimental data with the line of best fit is shown in Fig. 10 (a) for internal heating and Fig. 10 (b) for a step change on the boundary. It should be noted that not all data was used to perform the fit and this was due to two errors:

1. The imperfect step change on the thermal boundary (step change only)
2. The imperfect insulation which allows heat transfer to ambient

An instantaneous step change is impossible to achieve and hence, there will always be an associated error. This error was minimised using the custom PID controller presented in section 3.1. with Fig. 7 showing that the system took ~ 10 s to stabilise on the new temperature. Fig. 10 (b) shows the large variations in the heat flux response during the first 10 s of the test which was omitted to reduce the error from fitting to this unrepresentative data.

The second reason data was omitted from the fit was due to imperfect insulation. Towards the end of the decay the heat flux failed to return perfectly to zero no matter how long the experiment was left. This was due to a very small amount of heat entering the system through the insulation from ambient conditions. No perfect insulation exists which can completely eliminate this heat transfer but to reduce the steady state error the final 10 % of the decay was omitted from the fit. This was deemed appropriate as it is more important to fit to the shape of the decay where the thermal diffusivity is in the exponential terms rather than the steady state decay value.

Fig. 10 shows the extremely good fit between the analytical equations and the recorded surface heat flux for both methods (a) and (b). Fig. 11 shows the experimental data for method (c), using the heat stored. The shaded area in Fig. 11, (b) shows the energy stored during the development of the steady state temperature profile. This represents the difference between the heat generated within the heater and the heat passed out of the surfaces of the heater over this time period.

6.0.1. Lithium-ion cell demonstration

A Kokam 5 Ah pouch cell (SLPB11543140H5) was chosen to demonstrate the technique on a lithium-ion cell. The test procedure was similar to the test procedure for the silicone heater, although there were two important differences as detailed below.

First, a square wave pulse drive cycle with an amplitude of 14 A and a time period of 24 s was used to produce close to constant heat generation [15]. By using a pulsing drive cycle the state-of-charge of the cell oscillates by a negligible amount around a constant, enabling a constant rate of heat generation to be achieved, and also cancels out the contributions from entropic heating within the cell.

The second difference was the use of additional temperature control plates to remove the thermal pathway out of the cell tabs as shown in Fig. 12. As the cell tabs are welded onto the current collectors, they have a good thermal connection to the active material and the ability to either input or withdraw a large amount of heat from the cell. To remove this potential source of error, two thermistors were used to record the temperature gradient along the tab with a PID temperature control system used to maintain $T_1 = T_2 - 0.1^oC$. This ensured that the heat flow out of the tabs was < 3 % of the total heat being generated within the cell.

7. Results and discussion

7.1. Silicone block heater

7.1.1. Reference methods (Control)

Table 1 presents the thermal properties which were determined through calorimetry and from matching the internal temperature profile. The density was calculated using measurements of the mass and volume which was used to calculate the thermal diffusivity. Each measurement was taken a minimum of five times to calculate the sample mean and standard deviation.

7.1.2. Novel methods

Table 2 shows the thermal properties measured using the three new techniques presented in this paper. The sample mean and standard deviation for each of these methods has been plotted in Fig. 13 assuming the measurements are samples from a normal distribution. Both the internal heating and step change on the boundary methods show a good match to the reference values from control methods, with −5.60 % and

−7.34 % differences respectively. Errors within 5 % are standard in the field [16] as within this tolerance, factors such as absolute temperature calibration, environmental fluctuations, voltage logging accuracy etc. compound to increase uncertainty.

The error from the energy stored method (in orange) is significantly larger at 11.4 %. This is highlighted by the offset in Fig. 13 which shows significant disagreement with the internal heating and the step change methods. This difference can be explained by understanding the differences between these methods. Both the internal heating and the step change on the boundary methods use the shape of the heat flux decay to calculate the thermal properties. The energy stored method differs because it uses the area contained beneath the decay curve to calculate the energy stored shown in Fig. 11(b), and thus requires the magnitude of the decay as well as its shape. The difficulty with this is that the magnitude of the heat flux response is dependent on precise calibration of the heat flux sensors. This is very difficult to practically achieve as the calibration of the heat flux sensors is a function of the thermal contact resistance in their setup. The energy stored method is therefore heavily dependent on this calibration. Any systematic error contained in their calibration would affect the decay magnitude but not affect the decay shape. The larger error is attributed to this experimental limitation.

7.1.3. Thermal conductivity

The direct measurement of thermal conductivity measured from a step change on the boundary is presented in Table 3 which shows a 21.35 % difference from the reference thermal conductivity. This measurement is taken by fitting the magnitude of the step change heat flux response to the analytical Equation [30]. Similarly to the energy stored method, this magnitude is dependent on the calibration of the heat flux sensors which results in a significant error in the measurement. Future work will aim to improve the absolute accuracy of the heat flux sensor calibration which will allow for accurate direct measurements of thermal conductivity.

Despite this, the thermal conductivity can still be calculated within accuracies ≈ 5 % using the direct measurements of thermal diffusivity from section 4.1.2. This is done through the relationship given by Equation [3] which can be rearranged to Equation [32] which allows the thermal conductivity to be calculated given, the thermal diffusivity, α, specific heat capacity, c_p, and density, ρ. Fig. 14 shows the comparison in accuracies between the direct measurement and the calculated values of thermal conductivity.

$$k = \alpha c_p \rho \tag{32}$$

7.2. Lithium-Ion cell demonstration

The tests were repeated on the Kokam 5 Ah pouch cell and are reported in Table 4. Only the thermal diffusivity methods (a) and (b) were performed as the others were not deemed sufficiently accurate. The measurements of thermal diffusivity were used to calculate the conductivity using measurements of specific heat capacity and density. Note that the standard deviation was not available for the specific heat capacity or density and so both the diffusivity and conductivity are reported here as having the same standard deviation.

The calculated thermal conductivity was compared with properties obtained through the constituent materials approach from Zhao *et al.* [17]. The calculation from using the constituent materials approach was significantly different and was 50.08 % for this particular cell. It is impossible to separate the error between the measurement methods but we know from the experiments on the silicone heater that the error from the internal heating and step change methods is likely to be within 10 %. There are also the assumptions of steady, uniform internal heating which are unlikely to be perfectly true in a real lithium-ion cell. In addition, there is the effect of the casing on the measurement though these are not expected to be significant. Investigating the exact magnitude of these errors is the focus of further research but this analysis does conclude a significant error in the constituent materials method. The large error in the constituent materials method can be attributed to incorrect assumptions used which are highlighted by Roe *et al.* [18].

7.3. Conclusion

The novel methods presented in this paper for measuring the thermal diffusivity and thermal conductivity of a lithium-ion pouch cell are significantly more accurate than any other method. The key advance is the use of symmetrical boundary conditions which ensure that heat transfer around the casing of the cell is minimised. This enhances the prediction and confidence in internal cell temperature gradients which improves the safety and modelling of battery packs.

Three methods are presented for measuring thermal diffusivity using the symmetrical boundary condition concept. The internal heating method (a) and the step change method (b) are shown to be very accurate with errors of −5.60 % and −7.34 % respectively. The third method using the energy stored (c) had an error of 11.40 % which is larger than the previous methods and can be attributed to the calibration of the heat flux sensors.

Two methods have been presented for determining the thermal conductivity; measure it directly using the step change method, or calculate it using the measured thermal diffusivity along with separate measurements of density and specific heat capacity. The direct measurement method was limited in its accuracy due to difficulty calibrating the heat flux sensors and had an error of 21.35 %. Calculating the thermal conductivity using the measured diffusivity however is more accurate with errors of −5.60 % and −7.34 % for methods (a) and (b) respectively.

The absolute calibration of the heat flux sensor had a large impact on the accuracy of the direct thermal conductivity measurements and measurement of the thermal diffusivity using the energy stored method (c). Both of these methods require the absolute heat flux to be known, which is in contrast to methods (a) and (b) which only require the shape of the heat flux decay. Calibrating the absolute heat flux proved especially challenging as the calibration changed on each setup by approximately 19 % from the varying thermal contact resistance on the surfaces of the sensor. Future work will focus on improving the repeatability of the calibration which should lead to more accurate direct measurements of thermal conductivity. Further, it must be the focus of research and development teams to reduce the complexity of the apparatus – only through this mechanism will the measurement method ever become well used in the battery industry.

Despite calibration issues with the heat flux sensor, methods (a) and (b) for measuring the thermal diffusivity proved accurate. This marks a significant improvement on all other methods known to the author as this overcomes a major source of error from non-1D heat flow. The increased accuracy of the measurements enables better predictions of internal temperature gradients which is vital for the safety and modelling of lithium-ion cells. Additionally, these improvements to the model's accuracy will result in more efficient, longer lasting battery packs which will reduce the carbon footprint of future battery packs.

CRediT authorship contribution statement

Gavin White: Conceptualization, Methodology, Software, Validation, Formal analysis, Investigation, Resources, Data curation, Writing – original draft, Writing – review & editing, Visualization, Project administration. **Alastair Hales:** Resources, Writing – original draft, Writing – review & editing, Supervision, Supervision. **Yatish Patel:** Software, Writing – review & editing, Supervision. **Gregory Offer:** Writing – review & editing, Supervision, Project administration, Funding acquisition.

Declaration of Competing Interest

The authors declare the following financial interests/personal

relationships which may be considered as potential competing interests - Imperial College Innovations Limited has submitted a patent with application number #GB2116173.2. The patent application contains the inventive steps as detailed in this manuscript.

Acknowledgements

The authors would like to thank the financial support from the EPSRC and Rolls Royce Ltd. for the iCASE sponsorship (voucher: 18000166). Alastair Hales, Yatish Patel and Gregory Offer supported this work in a supervisory role.

Appendix

This appendix details a basic analysis of the heat transfer inside of a pouch cell. The analysis aims to validate a key assumption made in the derivation of the new methods – that the heat transfer through the thickness of a pouch cell can be modelled as 1D under the applied boundary conditions. A source of multi-dimensional heat transfer that could not be controlled through external boundary conditions is the heat transfer between layers at the current collector weld. Consider the cross-section of a pouch cell, shown in Fig. 15, where the layers of each current collector are welded to the tab. This presents two thermal pathways between points 1 and 3:

- A: Heat transfer through the layers from point 1 to point 3
- B: Heat transfer along the layers from point 1 to point 2 to point 3

The two pathways are highlighted in Fig. 16 and they can be analysed using the thermal resistance concept. Although this is an over-simplification of the heat transfer, it is useful for showing the rough proportion of heat transfer through each pathway. A cubic finite volume was then used to evaluate the pathways using the data available for the Kokam 5 Ah cell studied in this paper. The thermal resistance was calculated using.

$$R_\theta = \frac{\Delta x}{A_1 k_\theta} \tag{33}$$

where R_θ is the thermal resistance [K/W], Δx is the distance between the two points [m], A_1 is the area normal to the heat flow direction [m^2] and k_θ is the average thermal conductivity in the direction of heat flow [W/m.K]. As the area on each side of a cubic volume is the same the area, A, cancels when calculating the proportion of thermal resistance in each pathway. The results are presented in Table 5.

This analysis shows that 89 % of the heat transfer will be through pathway A – through the layers of the cell. This is including the assumption that there is no current collector to current collector thermal resistance. In reality there will be a significant thermal resistance at the weld between the current collectors which will increase the overall thermal resistance of pathway B further. It should also be noted that this cell, the Kokam 5 Ah, is a very high-power cell and the current collectors are almost at maximum thickness for a commercial cell. In a typical power or energy-dense cell this error will be reduced further. This analysis is heavily simplified but the relative magnitude of the results gives us confidence in the assumption of 1D heat transfer and the methods we have developed in this paper.

References

[1] L. Lander, E. Kallitsis, A. Hales, J.S. Edge, A. Korre, G. Offer, Cost and carbon footprint reduction of electric vehicle lithium-ion batteries through efficient thermal management, Appl. Energy 289 (2021), 116737, https://doi.org/10.1016/j.apenergy.2021.116737.

[2] M.P. Klein, J.W. Park, Current Distribution Measurements in Parallel-Connected Lithium-Ion Cylindrical Cells under Non-Uniform Temperature Conditions, J. Electrochem. Soc. 164 (2017) A1893–A1906, https://doi.org/10.1149/2.0011709jes.

[3] I.A. Hunt, Y. Zhao, Y. Patel, J. Offer, Surface Cooling Causes Accelerated Degradation Compared to Tab Cooling for Lithium-Ion Pouch Cells, J. Electrochem. Soc. 163 (2016) A1846–A1852, https://doi.org/10.1149/2.0361609JES.

[4] F.P. Incropera, D.P. Dewitt, T.L. Bergman, A.S. Lavine, Foundations of Heat Transfer, 6th ed., John Wiley & Sons, Singapore, 2012.

[5] D. Bernardi, E. Pawlikowski, J. Newman, A General Energy Balance for Battery Systems, J. Electrochem. Soc. 132 (1) (1985) 5–12.

[6] M. Steinhardt, J.V. Barreras, H. Ruan, B. Wu, G.J. Offer, A. Jossen, Meta-analysis of experimental results for heat capacity and thermal conductivity in lithium-ion batteries: A critical review, J. Power Sources 522 (2022) 230829.

[7] V. Vishwakarma, C. Waghela, Z. Wei, R. Prasher, S.C. Nagpure, J. Li, F. Liu, C. Daniel, A. Jain, Heat transfer enhancement in a lithium-ion cell through improved material-level thermal transport, J. Power Sources 300 (2015) 123–131, https://doi.org/10.1016/j.jpowsour.2015.09.028.

[8] S.J. Bazinski, X. Wang, Experimental study on the influence of temperature and state-of-charge on the thermophysical properties of an LFP pouch cell, J. Power Sources 293 (2015) 283–291, https://doi.org/10.1016/j.jpowsour.2015.05.084.

[9] D. Werner, A. Loges, D.J. Becker, T. Wetzel, Thermal conductivity of Li-ion batteries and their electrode configurations – A novel combination of modelling and experimental approach, Journal of Power Sources. 364 (2017) 72–83. https://doi.org/https://doi.org/10.1016/j.jpowsour.2017.07.105.

[10] H. Maleki, S.A. Hallaj, J.R. Selman, R.B. Dinwiddie, H. Wang, Thermal Properties of Lithium-Ion Battery and Components, Journal of The Electrochemical, Society. 146 (3) (1999) 947–954.

[11] W.J. Parker, R.J. Jenkins, C.P. Butler, G.L. Abbott, Flash Method of Determining Thermal Diffusivity, Heat Capacity, and Thermal Conductivity, J. Appl. Phys. 32 (1961) 1679–1684, https://doi.org/10.1063/1.1728417.

[12] M. Steinhardt, E.I. Gillich, M. Stiegler, A. Jossen, Thermal conductivity inside prismatic lithium-ion cells with dependencies on temperature and external compression pressure, J. Storage Mater. 32 (2020), 101680, https://doi.org/10.1016/j.est.2020.101680.

[13] L.S. Fletcher, Recent Developments in Contact Conductance Heat Transfer, J. Heat Transfer 110 (1988) 1059–1070, https://doi.org/10.1115/1.3250610.

[14] M. Newville, T. Stensitzki, D.B. Allen, A. Ingargiola, LMFIT: Non-Linear Least-Square Minimization and Curve-Fitting for Python, (2014). https://doi.org/10.5281/ZENODO.11813.

[15] A. Hales, R. Prosser, L. Bravo Diaz, G. White, Y. Patel, G. Offer, The Cell Cooling Coefficient as a design tool to optimise thermal management of lithium-ion cells in battery packs, ETransportation. 6 (2020), 100089, https://doi.org/10.1016/J.ETRAN.2020.100089.

[16] Thermal performance - NPL, (n.d.). https://www.npl.co.uk/products-services/advanced-materials/thermal-performance (accessed November 11, 2021).

[17] Y. Zhao, Y. Patel, T. Zhang, G.J. Offer, Modeling the Effects of Thermal Gradients Induced by Tab and Surface Cooling on Lithium Ion Cell Performance, J. Electrochem. Soc. 165 (2018) A3169–A3178, https://doi.org/10.1149/2.0901813JES.

[18] C. Roe, X. Feng, G. White, R. Li, H. Wang, X. Rui, C. Li, F. Zhang, V. Null, M. Parkes, Y. Patel, Y. Wang, H. Wang, M. Ouyang, G. Offer, B. Wu, Immersion cooling for lithium-ion batteries – a review, J. Power Sources 525 (2022), 231094, https://doi.org/10.1016/j.jpowsour.2022.231094.